4

Monte Carlo Simulation for Ion Implantation Profiles, Amorphous Layer Thickness Formed by the Ion Implantation, and Database Based on Pearson Function

Kunihiro Suzuki
Fujitsu Laboratories Ltd.
Japan

1. Introduction

Ion implantation is a standard technology to dope substrates in Si VLSI processes. The ion implantation profiles in Si substrates are generated based on a vast secondary ion mass spectrometry (SIMS) database of ion implantation profiles in commercial simulators such as Sentaurus Process. However, we cannot predict profiles accurately when there are no experimental data or only poor data. Recently, various ions such as C, N, and F have been used to suppress transient enhanced diffusion in the subsequent annealing processes, as shown by Hu (2000) and Mirabera (2005). Furthermore, various substrates have been investigated, such as SiGe for state of the art Si LSI [Kim (2006), Weber (2007)], Ge for post Si devices [Chui (2002), Shang (2003)], and SiC for high-temperature, high-voltage, and high-power applicants [Schoerner (1999)]. Ion implantation is also a standard technology to dope these substrates. However, accumulation of the corresponding experimental database is time and cost consuming. Therefore, theoretical evaluation of these profiles is invoked.

Monte Carlo (MC) simulation is widely used for predicting ion implantation profiles and has long been developed to be available for any combination of incident ion and substrate atoms [Ziegler (2008) SRIM, Tian (2003), Suzuki (2009)]. We can evaluate the accuracy of the MC by comparing an ion implantation database such as FabMeister-IM [Suzuki (2010a)]. We show that the MC results sometimes deviate from the experimental data with its original form. We modified the electron stopping power model, calibrated its parameters, and reproduced most of the database with the energy range between 0.5 and 2000 keV.

MC simulation takes long time to calculate the profiles, and the profiles are scattered in the low concentration region. Therefore, MC results are sometimes converted to an analytical Pearson function presented by Hofker (1975) and Ashworth (1990) utilizing its moment parameters, with which we can expect smooth profiles over the entire region. Furthermore, we can use the moment parameters of MC as a database and can instantaneously obtain profiles using the Pearson function for various ion implantation conditions by interpolating the moment parameter values. However, we show that direct use of the moment parameters evaluated from MC data sometimes induces inaccurate Pearson function, as shown in

Suzuki (2010b). We show the way for obtaining moment parameters to reproduce MC results using Pearson function.
Amorphous layer is formed by the ion implantation. This amorphous layer is utilized to obtain shallow junctions by suppressing channelling effect. B ions implanted into substrates with and without an amorphous layer formed by Ge ion implantation are shown in Suzuki (2010a). If an amorphous layer is formed and ion implantation is used to add impurities into this amorphous layer, a significant shallow junction can be obtained with no channelling tail.
Furthermore, the B activation phenomenon becomes to be drastically changed where the amorphous layer is formed or not. The sheet resistance with annealing time at 600°C in substrates with an amorphous layer formed by Ge ion implantation is significantly reduced compared to that without forming an amorphous layer [Suzuki (2004)]. These results show that by forming an amorphous layer and allowing it to recrystallize at a low temperature, it is possible to obtain low resistivity over a wide time range. It has been confirmed that this phenomenon is not intrinsic to Ge and can also be observed in amorphous layers formed by other impurities where recrystallization is allowed to take place at temperatures that produce little redistribution of impurities [Solmi (1990), Jin (2002), Suzuki (2003), Pawlak (2005)]. Therefore, it is also very important to predict the amorphous layer thickness depending on various ion implantation conditions.
MC simulation also has information on energy transferred to the substrate atoms, that is, induced damage, and the damage has been related to the amorphous layer thickness [Hobler (1988), Cerva(1992)]. Prussin (1984) also analyzed the formation of the continuous amorphous layer based on Brice's energy deposition model [Brice (1975)]. We also show that the amorphous layer thickness can also be predicted by MC using a critical vacancy concentration.

2. Experiments

We deposited around 1 μm of Si by low pressure chemical vapour deposition at 550°C on Si substrates or formed an amorphous layer by Ge ion implantation. We verified that the profiles near the peak and surface regions in these amorphous layers are almost the same as the profiles in crystal Si (cSi) substrates. Therefore, we also used the profiles in cSi, neglecting the channelling tail region to evaluate the accuracy of MC results.
We evaluated ion implanted impurity concentration profiles using SIMS. In the SIMS measurement, the primary ions were raster scanned over a wide area, and secondary ions were collected from the central small area using electronic gating to avoid edge effects. The depth calibration of the measured profile was done using a Dektak 2A surface profilometer, and the concentration scale was adjusted to the as-implanted dose. The standard SIMS measurement conditions are shown in ref. [Suzuki (1998)]. The accurate SIMS measurement for ultra shallow profiles has been developed by [Kataoka (2007), Tada (2008)], which enables us to compare SIMS and MC in a low ion implantation energy region of around 1 keV.
We also evaluated the amorphous layer thickness by transmission electron microscopy (TEM). TEM measurements were performed using a JEOL 2500 transmission electron microscope operating at 200 keV. Cross-sectional view specimens were obtained by ion milling [Suzuki (2006)].

3. Brief review of the physics of ion implantation

We will briefly explain the physics of ion implantation. A detailed description can be found in Ziegler (2008).
In a nuclear interaction, a binary interaction is assumed. The energy transferred from the incident atom to the target atom T_{2f} is given by

$$T_{2f} = \frac{4M_1M_2}{(M_1+M_2)^2}\sin^2\left(\frac{\Phi}{2}\right)T_{1i}, \tag{1}$$

where T_{1i} is the incident atom energy, and M_1 and M_2 are the incident and target atom mass numbers, respectively. Φ is the scattering angle calculated using Ziegler-Litmark-Biersak universal potential model [Ziegler (2008)].
On the other hand, Lindhard proposed an electron stopping power of

$$S_e = r_e 1.21\times10^{-16} Z_1^{1/6}\frac{Z_1Z_2}{\left(Z_1^{2/3}+Z_2^{2/3}\right)^{3/2}}\frac{1}{\sqrt{M_1[g]}}\sqrt{E[eV]}\quad\left[eV\bullet cm^2\right], \tag{2}$$

where Z_1 and Z_2 are the incident and target atomic numbers, respectively [Lindhard (1961)]. r_e is a fitting parameter. Lindhard's S_e model of Eq. 2 assumes the interaction between the electron cloud of ions and substrate atoms. However, the electron cloud of incident ions is expected to be stripped at high-energy regions. Therefore, Lindhard's model becomes invalid at high-energy regions.
Bethe derived an electron stopping power model, which is valid at high-energy regions, where the electron cloud is completely stripped as [Bethe (1930)]

$$S_e(E) = \left(\frac{q^2}{4\pi\varepsilon_0}\right)^2\frac{2\pi M_1Z_2{Z_1}^2}{m_eE}\ln\left(\frac{4m_eE}{I\,M_1}\right), \tag{3}$$

where q is the electron charge, ε_0 is the permittivity in vacuum, m_e is the electron mass, and I is the average electron excitation energy, and it is given in an empirical form as [Dalton (1968)]

$$I = \begin{cases} 11.2+11.7Z_2 & for\ Z_2 \le 13 \\ 52.8+8.71Z_2 & for\ Z_2 > 13 \end{cases} \tag{4}$$

We propose to combine Lindhard's model with Bethe's model as follows.
First, Bethe's model is invalid in low-energy regions, and we modify it not to influence Lindhard's model in low-energy regions. The energy where Bethe's model has a maximum value can be evaluated from $\partial S_e/\partial E = 0$, and we obtain

$$E = eE_r, \tag{5}$$

where e is the base of natural logarithm, and

$$E_r = \frac{M_1}{4m_e}I. \tag{6}$$

We modify Bethe's model $S_{e\_mB}(E)$ as

$$S_{e\_mB}(E)=\begin{cases}\left(\frac{q^2}{4\pi\varepsilon_0}\right)^2\frac{2\pi M_1 Z_2 {Z_1}^2}{m_e e E_r} & for\ E\le eE_r\\ \left(\frac{q^2}{4\pi\varepsilon_0}\right)^2\frac{2\pi M_1 Z_2 {Z_1}^2}{m_e E}\ln\left(\frac{E}{E_r}\right) & for\ E>eE_r\end{cases}. \quad (7)$$

Biersack et al. proposed a model similar to Eq. 7 with a mathematical trick [Biersack (1980)]. Both modified Bethe's models become the original Bethe's model at high-energy regions and much larger than Lindhard's model at low-energy regions. We propose to combine Lindhard's model and the modified Bethe's model of Eq. 7 as [Suzuki (2009)]

$$\frac{1}{S_e}=\left[\left(\frac{1}{r_e S_{eL}}\right)^{\theta}+\left(\frac{1}{r_{eh}S_{e\_mB}}\right)^{\theta}\right]^{1/\theta}. \quad (8)$$

We also introduce a fitting parameter r_{eh} for generality although we use r_{eh} of 1 in this analysis. (We need experimental data in the energy region much larger than eE_r to calibrate r_{eh}, which we have none here). This S_e becomes Lindhard's model at low-energy regions, and Bethe's model at high-energy regions. When θ is one, it is the same form of the Biersack's model [Biersack (1980)]. θ empirically expresses the transition from Lindhard's model to Bethe's model.

Figure 1 shows the dependence of S_e of B in Si on θ. The interaction between both models becomes significant with decreasing θ. We can evaluate S_e of B by varying the value of θ in the MeV energy region. It is also clear that we cannot evaluate robustly r_{eh} with the experimental data less than 10000 keV.

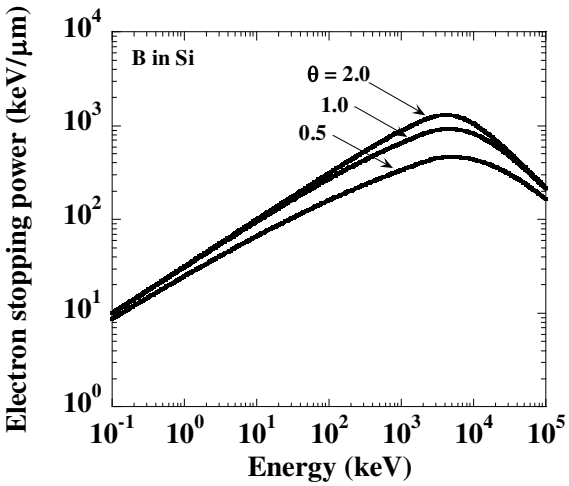

Fig. 1. Dependence of S_e of B in Si substrate on θ.

We can evaluate the energy transferred to the substrate atom of T_{2f} given by Eq. 1. The recoiled atoms are generated if the T_{2f} is larger than the critical displacement energy E_d. We then trace trajectories of the recoiled atom with the energy of $T_{2f} - E_d$ and count up the vacancies generated by the recoiled atom.

Modified Kinchin-Peace model is commonly applied to the primary recoiled atoms instead of tracing the recoiled substrate atom to save computation time [Ziegler (2008)]. The number of vacancy is evaluated using an analytical formula as a function of T_{2f}, and it is recorded at the location of the primary recoiled position. In this treatment, the damage (vacancy) can be expressed by

$$\nu = \begin{cases} 0.4\dfrac{T_{2f}}{E_d} & for\ T_{2f} \geq 2.5E_d \\ \dfrac{T_{2f}}{E_d} & for\ E_d \leq T_{2f} < 2.5E_d \\ 0 & for\ T_{2f} < E_d \end{cases} \tag{9}$$

The transferred energy is not perfectly consumed by nuclear interaction, but some are consumed through the electron stopping power during many collisions. To ensure the assumption, the term of 0.4 is added in the first term of Eq. 9. E_d is an important parameter that control the radiation damage, but the experimental methods show widely varying results for E_d of Si substrate in the range of 10-30 eV, and theoretical evaluation shows that it depends on the direction of recoiled atom in the lattice and also in the range between 12 and 36 eV and average of around 24 eV [Holmstrom (2008)]. We used E_d = 25 eV for both Si and Ge substrates in this analysis. This value influences the vacancy concentration, but the similar results can be expected using different E_d values.

We implemented the above physics in our own Monte Carlo simulator [Suzuki 2009]. We can switch two modes for evaluating the vacancy concentration: one is not tracing the recoiled substrate atom and use Eq. 10, and the other one is tracing the recoiled substrate atom trajectories. The former is called non-tracing mode, and the latter tracing mode is denoted by T.

4. Comparison of MC with SIMS data

Figure 2 shows the comparison of SIMS and MC data with r_e of 1 for B, P, and As implantation. We obtained good agreement between MC and SIMS data for As profiles, and close agreement for P profiles, but significant deviation for B profiles. This may mean that we cannot expect predictive results from MC simulation since we cannot have clear physical reason whether our calculation for new ion in a certain substrate is like As or B profiles.

Figures 3 compares SIMS and MC B data with various r_e. The profile becomes shallower with increasing r_e. We can obtain close agreement of peak position as well as the overall shape of the profile with r_e of around 1.5.

Figure 4 compares various energy-dependent B SIMS profile data with the MC simulation with optimized r_e of 1.55. It is noteworthy that we can fit the data with a single r_e over a wide energy range.

We obtained a similar agreement for As SIMS data for various energies as shown in Fig. 5 using r_e of 1.0 as the same value in Fig. 2. The default value of r_e of 1 is also valid for various energies for As.

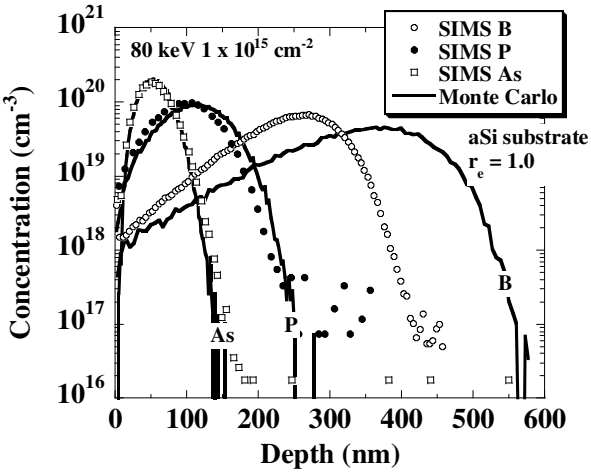

Fig. 2. Comparison of MC with SIMS data with r_e =1.

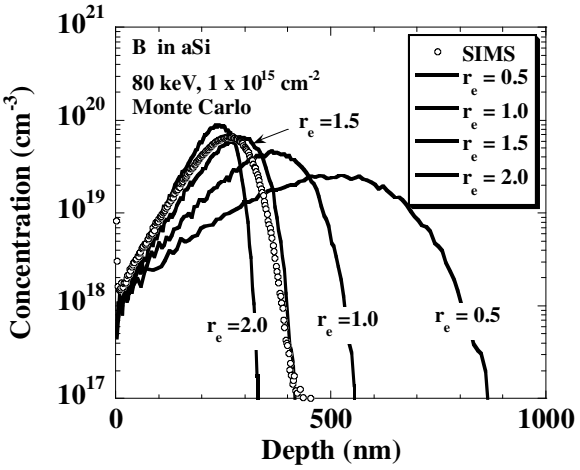

Fig. 3. Comparison of MC with B SIMS data at different values of r_e.

We obtained the similar results for the other ions of In, Sb, Ga, Ge, Si, N, F, and C in Si substrate, and B, P, and As in Ge substrate, and further in Mo, HfO_2, and photo-resist substrates by tuning corresponding r_e that is valid for various energies, which is shown in [Suzuki (2009)]. Table 1 summarizes optimized r_e. The values of r_e are not far from 1 and it is 1 in many cases. Therefore, we can predict the profiles in an amorphous layer using a MC simulation with a default r_e deduced from the table, and we can further improve the accuracy if we tune r_e with some experimental data.

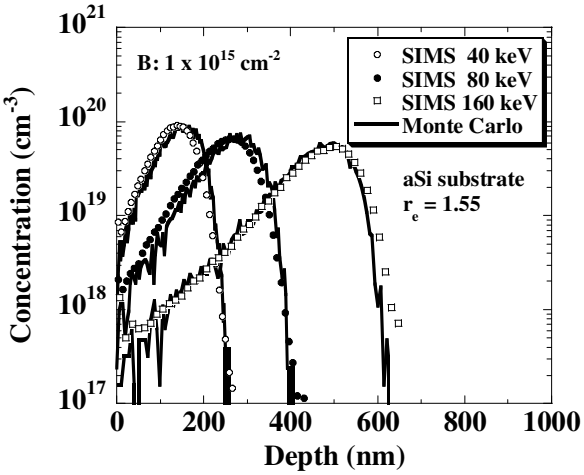

Fig. 4. Comparison of SIMS B profiles with MC with optimized r_e = 1.55.

		Z_2						
		01:H	06:C	08:O	14:Si	32:Ge	42:Mo	72:Hf
Z_1	05:B	1.0	1.7	0.8	1.55	1.0	1.0	3.0
	06:C	---	---	---	1.5	---	---	---
	07:N	---	---	---	1.4	---	---	---
	09:F	---	---	---	1.0	---	---	---
	14:Si	---	---	---	1.25	1.0	---	---
	15:P	1.0	1.0	1.0	1.2	1.0	1.0	1.0
	32:Ge	---	---	---	1.0	---	---	---
	33:As	---	---	0.5	1.0	1.0	---	1.0
	49:In	---	---	---	1.0	---	---	---
	51:Sb	---	---	---	1.0	---	---	---

Table 1. r_e for various incident ion and substrate atoms.

Low-energy ion implantation of around 1 keV is frequently used to realize shallow junctions. There is no critical point at this energy region from the standpoint of physics. However, SIMS reaches its resolution limit in this energy region. Therefore, the accuracy of the MC simulation in low-energy region has not been robustly evaluated. Recently, fundamental SIMS measurement mechanisms have been understood, and their accuracy have also been improved [Kataoka (2007), Tada (2008)]. Therefore, it is interesting to compare these SIMS data with the calibrated MC simulation. Figure 6 compares the SIMS B and As profiles and MC simulation. The SIMS B and As profiles near the peak region agree well with the MC data. Therefore, the MC simulation calibrated in the energy range of around few 10 keV can also predict the profiles in the energy range of around 1 keV.
Figure 7 also compares SIMS and MC results with combined S_e model of Eq. 8. We applied θ of 1.65 to the other energies and ions and obtained good agreement. We therefore can predict ion implantation profiles over the energy region from 0.5 keV to more than 2000 keV with our MC.

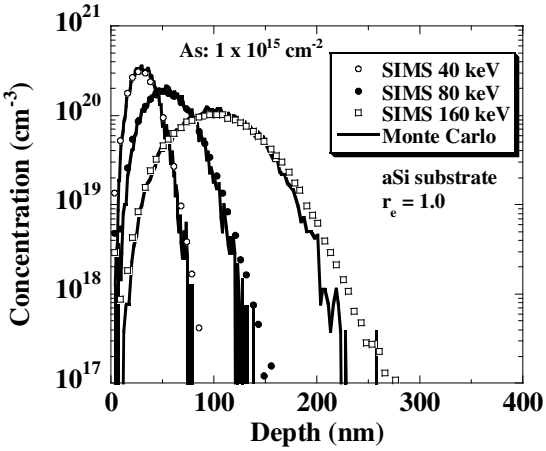

Fig. 5. Comparison of SIMS As profiles with MC with default r_e of 1.0.

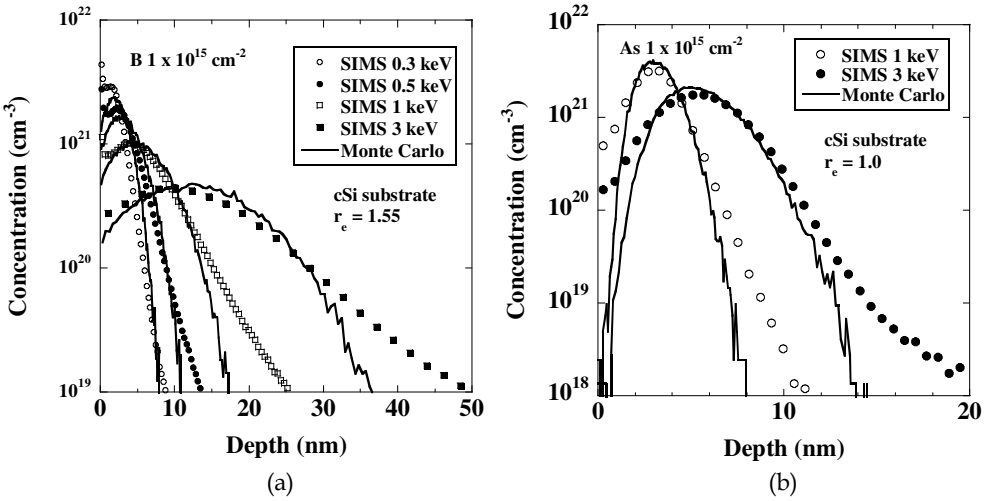

Fig. 6. Comparison of low-energy B and As SIMS profiles with MC.

Ziegler utilized the linear response method and treated the transition from Lindhard's model to Bethe's model more universally [Ziegler (2008)]. Although the Ziegler's model is physical one, we cannot obtain a good agreement as it is [Suzuki (2009)] and tune its parameters, which is not easy to handle.

As we pointed out in the Section 3, the Lindhard's S_e model becomes invalid in high-energy region, especially for B in the practical high-energy region of around MeV. Figure 7 compares B SIMS data with the MC simulation using Lindhard's S_e model. SIMS and MC results agree well at 400 keV. However, Lindhard's model predicts much shallower B profiles at 1200 and 2000 keV.

Figure 8 shows the dependence of stopping powers on energy. We need not care about this subject of the limitation of Lindhard's S_e model for P and As since eE_r values are much

larger than 5 MeV for P and As, as shown in Fig. 8. However, if we use much higher energies for these ions or light ions such as B, we should find optimal values of θ for each combination of ion and substrate and may be r_{eh} since the model is empirical.

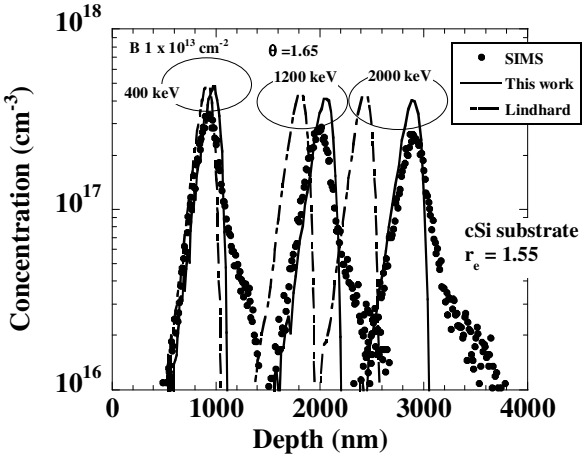

Fig. 7. Comparison of high-energy B SIMS data with MC using Lindhard and combined Se models.

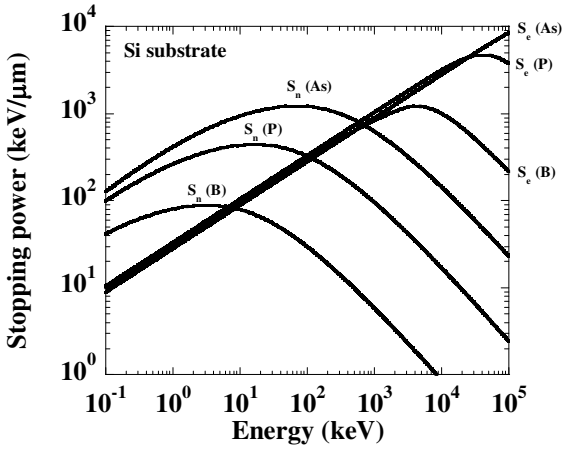

Fig. 8. Stopping powers of B, P, and As in Si substrate.

5. Database based on Pearson function

MC results are scattered in the low concentration region, and hence analytical fitting function such as Pearson IV is sometimes used instead of the MC raw data. Furthermore, if we convert the results to an analytical function, we can establish the database based on the parameters of the function and generate profiles for any ion implantation conditions by

interpolating the parameter values. In these cases, it is important how the analytical function can reproduce the MC results. Pearson function is vital, and hence it is a standard function to express ion implantation profiles. The parameters of the function can be evaluated from first four moments of the MC results. We show here that the simple use of the raw moments of the MC results sometimes induce significant error and how to solve it. Pearson IV is frequently predominately used among the Pearson function family. There exists long-standing discussion on validity of the selective use of Pearson IV [Ashworth (1990)]. We give some insight on it.

5.1 Pearson function family

Here, we briefly explain Pearson function family [Ashworth (1990), Selberherr (1984)] and show the definition of moments of the profiles and the relation of the moments to the Pearson function parameters.

We first convert the raw profile $N(x)$ to the normalized one $h(x)$ with respect to the dose for simple treatment, that is,

$$h(x) = \frac{N(x)}{\int_{x_a}^{x_b} N(x)dx} \tag{10}$$

Although the definition region is infinite plane for Pearson IV function, it is limited for some Pearson functions, and we hence describe the definition region as $[x_a, x_b]$

The first moment parameter of projected range R_p is defined as

$$R_p = \int_{x_a}^{x_b} xh(x)dx \tag{11}$$

We convert the depth x with respect to R_p to s as

$$s = x - R_p \tag{12}$$

We also define $s_a \equiv x_a - R_p, s_b \equiv x_b - R_p$.

The n-th moment μ_n can be evaluated as

$$\mu_n = \int_{s_a}^{s_b} s^n h(s)ds \tag{13}$$

Instead of the moments of μ_2, μ_3, μ_4 defined by Eq. 13, the following related parameters are used.

$$\Delta R_p = \sqrt{\mu_2} \tag{14}$$

$$\gamma = \frac{\mu_3}{\Delta R_p{}^3} \tag{15}$$

$$\beta = \frac{\mu_4}{\Delta R_p{}^4} \tag{16}$$

ΔR_p is called as straggling; γ, as skewness; and β, as kurtosis.
Pearson function family is generated from the differential equation

$$\frac{dh}{ds} = \frac{(s-a)h}{b_0 + b_1 s + b_2 s^2} \tag{17}$$

Modifying Eq. 17 to

$$\left(b_0 + b_1 s + b_2 s^2\right)\frac{dh}{ds} = (s-a)h \tag{18}$$

multiplying s^n, and integrating it in the region of $[s_a, s_b]$, we obtain

$$\int_{s_a}^{s_b}\left(b_0 s^n + b_1 s^{n+1} + b_2 s^{n+2}\right)\frac{dh}{ds}ds = \int_{s_a}^{s_b}\left(s^{n+1} - as^n\right)hds \tag{19}$$

We then obtain

$$\left[\left(b_0 s^n + b_1 s^{n+1} + b_2 s^{n+2}\right)h\right]_{s_a}^{s_b} - \int_{s_a}^{s_b}\left(nb_0 s^{n-1} + (n+1)b_1 s^n + (n+2)b_2 s^{n+1}\right)hds = \int_{s_a}^{s_b}\left(s^{n+1} - as^n\right)hds \tag{20}$$

Imposing

$$\lim_{s \to s_a, s_b}\left[s^{n+2}h\right] = 0 \tag{21}$$

we obtain

$$nb_0\mu_{n-1} + \left[(n+1)b_1 - a\right]\mu_n + \left[(n+2)b_1 + 1\right]\mu_{n+1} = 0 \tag{22}$$

Substituting n = 0, 1, 2, 3 in Eq. 22, and utilizing $\mu_0 = 1, \mu_1 = 0$, each parameter in Eq. 17 can be expressed with the moment parameters as

$$b_0 = -\frac{4\beta - 3\gamma^2}{A}\Delta R_p{}^2 \tag{23}$$

$$b_1 = -\frac{\beta + 3}{A}\gamma\Delta R_p \tag{24}$$

$$b_2 = -\frac{2\beta - 3\gamma^2 - 6}{A} \tag{25}$$

$$a = b_1, \tag{26}$$

where

$$A = 10\beta - 12\gamma^2 - 18 \tag{27}$$

The definition region of $[s_a, s_b]$ is related to the singular points of the denominator of Eq. 17. When the denominator is first order equation with respect to s, that is $b_2 = 0$, the related singular point ξ_s is

$$\xi_s = -\frac{b_0}{b_1} \tag{28}$$

When the denominator is second order equation with respect to s, that is $b_2 \neq 0$, the related singular points ξ_1, ξ_2 are

$$\xi_1 = \frac{-b_1 - \sqrt{b_1^2 - 4b_0 b_2}}{2b_2} \tag{29}$$

$$\xi_2 = \frac{-b_1 + \sqrt{b_1^2 - 4b_0 b_2}}{2b_2} \tag{30}$$

When the denominator has double roots, the related singular point ξ_D is

$$\xi_D = -\frac{b_1}{2b_2} \tag{31}$$

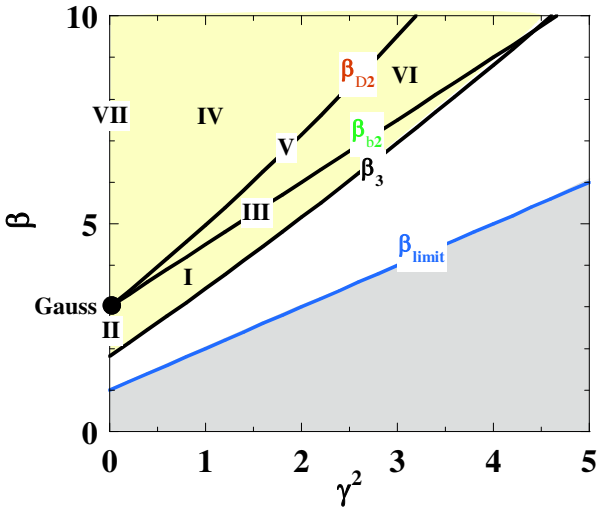

Fig. 9. Domains for each Pearson function. Any function that is always positive, concentrantion should be $\beta > \beta_{limit}$

Figure 11 shows the domains for various Pearson functions in (γ^2, β) plane, where

$$\beta_{D2} = \frac{3\left(13\gamma^2 + 16\right) + 6\left(\gamma^2 + 4\right)^{\frac{3}{2}}}{32 - \gamma^2} \tag{32}$$

$$\beta_{b2} = \frac{3}{2}\gamma^2 + 3 \tag{33}$$

$$\beta_3 = \frac{9\left[6\gamma^2 + 5 + \sqrt{\frac{9}{16}\gamma^6 + 8\gamma^4 + 25\left(\gamma^2 + 1\right)}\right]}{50 - \gamma^2} \tag{34}$$

$$\beta_{limit} = \gamma^2 + 1 \tag{35}$$

β_3 is the limit for Pearson function, and β_{limit} is the limitation for general distribution function that holds positive over entire definition region [Ashworth (1990)].
The corresponding $\left(\gamma^2, \beta\right)$ region, definition region $\left[s_a, s_b\right]$, and analytical form of each Pearson function are as follows [Ashworth (1990)].
Gauss: $\gamma = 0, \beta = 3; \left[-\infty, \infty\right]$

$$\ln h(s) = \frac{s^2}{2b_0} + \ln K \text{ ,} \tag{36}$$

where K is the factor to realize normalization, and it is also used for the other functions.
Pearson IV, VII: $\beta > \beta_{D2}; \left[-\infty, \infty\right]$
The expression for Pearson IV is given by

$$\ln h(s) = \frac{1}{2b_2}\ln\left|b_0 + b_1 s + b_2 s^2\right| - \frac{2b_1 + \frac{b_1}{b_2}}{\sqrt{4b_0 b_2 - {b_1}^2}}\tan^{-1}\left(\frac{2b_2 s^2 + b_1}{\sqrt{4b_0 b_2 - {b_1}^2}}\right) + \ln K \tag{37}$$

Pearson VII is the special case of Pearson IV, where $\gamma = 0$, that is, identical to $b_1 = 0$ in Eq. 37 and hence the expression for Pearson VII is given by

$$\ln h(s) = \frac{1}{2b_2}\ln\left|b_0 + b_2 s^2\right| + \ln K \tag{38}$$

Pearson V: $\beta = \beta_{D2}; \left[-\infty, \xi_D\right]$ *for* $\gamma < 0, \left[\xi_D, \infty\right]$ *for* $\gamma > 0$

$$\ln h(s) = \frac{1}{2b_2}\ln\left|b_0 + b_1 s + b_2 s^2\right| + \frac{2b_1 + \frac{b_1}{b_2}}{2b_2 s + b_1} + \ln K \tag{39}$$

Pearson VI: $\beta_{b2} < \beta < \beta_{D2}; \left[-\infty, \xi_1\right]$ *for* $\gamma < 0, \left[\xi_2, \infty\right]$ *for* $\gamma > 0$

$$\ln h(s) = \frac{1}{2b_2}\ln\left|b_0 + b_1 s + b_2 s^2\right| - \frac{b_1 + \frac{b_1}{2b_2}}{\sqrt{4b_0 b_2 - {b_1}^2}}\ln\left|\frac{2b_2 + b_1 - \sqrt{{b_1}^2 - 4b_0 b_2}}{2b_2 + b_1 + \sqrt{{b_1}^2 - 4b_0 b_2}}\right| + \ln K \tag{40}$$

Pearson I, II: $\beta_3 < \beta < \beta_{b2}; \left[\xi_1, \xi_2\right]$
The expression of Pearson I is the same as that for Pearson VI given by

$$\ln h(s) = \frac{1}{2b_2}\ln\left|b_0 + b_1 s + b_2 s^2\right| - \frac{b_1 + \frac{b_1}{2b_2}}{\sqrt{4b_0 b_2 - {b_1}^2}}\ln\left|\frac{2b_2 + b_1 - \sqrt{{b_1}^2 - 4b_0 b_2}}{2b_2 + b_1 + \sqrt{{b_1}^2 - 4b_0 b_2}}\right| + \ln K \tag{41}$$

Pearson I is the special case of Pearson I, where $\gamma = 0$, that is $b_1 = 0$ in Eq. 41, and is given by

$$\ln h(s) = \frac{1}{2b_2}\ln\left|b_0 + b_2 s^2\right| + \ln K \tag{42}$$

Pearson III: $\beta = \beta_{b2}; [-\infty, \xi_s]$ *for* $\gamma < 0, [\xi_s, \infty]$ *for* $\gamma > 0$

$$\ln h(s) = \frac{1}{b_1}s - \left(1 + \frac{b_0}{{b_1}^2}\right)\ln\left|s + \frac{b_0}{b_1}\right| + \ln K \tag{43}$$

It seems that we can simply obtain the moments of MC results, and select the function and generate the corresponding Pearson function. However, there are some problems in this procedure, as shown in the following sections.

5.2 Monte Carlo tracing to the negative plane

When light impurities are ion-implanted into a substrate composed of heavy atoms, the backscattering becomes significant, and the number of them is not negligible. The resultant profiles are cut at the surface. On the other hand, the Pearson profile is continuous over the whole area. Therefore, the moments of this MC result cut at the surface may induce inaccurate Pearson distribution.

Figure 10 shows B profiles ion-implanted in W substrates. It clearly shows that the back scattering is significant and the profiles are cut at the surface. The dashed line corresponds to the Pearson profiles using the moments of the MC results. The agreement is not as good as expected.

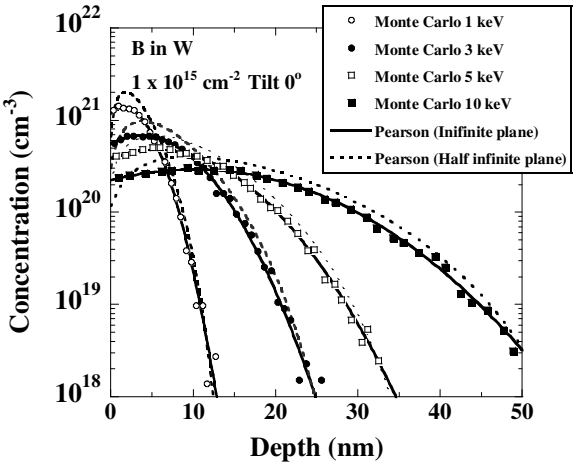

Fig. 10. MC simulation of B ion implantation profiles in W substrates. Pearson function using raw moment parameters, and moment parameters of MC tracing to the negative plane are also shown.

This situation occurs when the energy becomes quite low even in cases of B in Si substrate although the backscattering is not so significant for energy regions of around few 10 keV.

Figure 11 shows the B profiles ion implanted at 0.5 keV. It is also clear that the back scattering is significant in this case, and the Pearson profile deviates from the MC result as is also the case in W substrate.

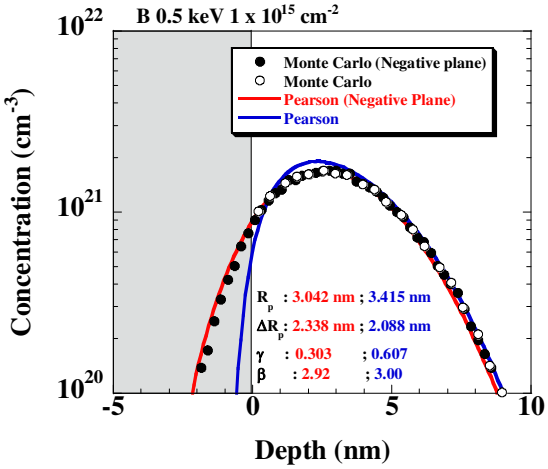

Fig. 11. MC simulation of B ion implantation profiles in Si substrates. Pearson function using raw moment parameters, and moment parameters of MC tracing to the negative plane are also shown.

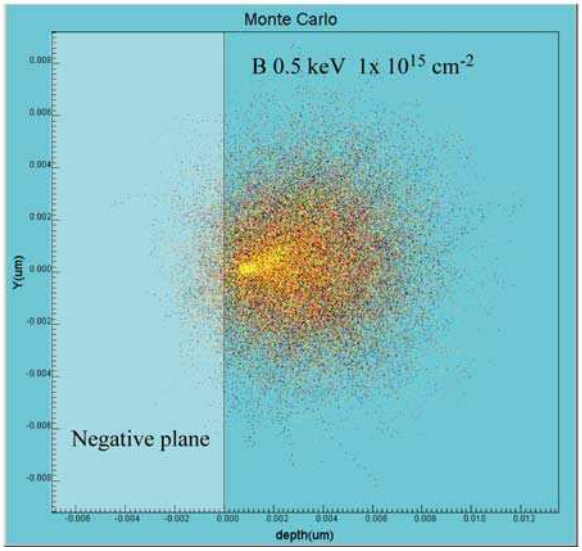

Fig. 12. MC tracing to the negative plane.

We propose virtually setting the substrate in a negative plane (infinite plane) and tracing ions that are backscattered at the surface or that have escaped from the bulk to the surface,

as shown in Fig. 12 [Suzuki (2010b)]. By extracting the moments from the results, we reproduced the MC results more accurately than in the case of the standard MC simulation moments, as shown in Figs. 10 and 11.

5.3 β at high-energy region

We can overcome the problem of backscattering by using MC tracing to the negative plane, as shown in the previous section. We also show the other problem here, which is more fundamental one related to the limitation of Pearson function. This is also related to the availability to use Pearson IV function among Pearson function family.

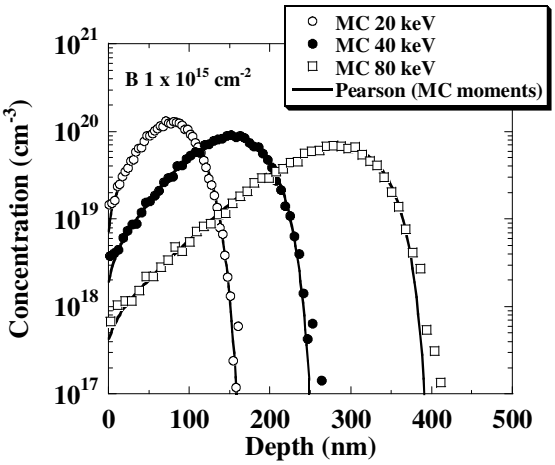

Fig. 13. MC simulation of B ion implantation profiles in Si substrates in the moderate-energy region between 20 and 80 keV. Pearson function using raw moment parameters, and moment parameters of MC tracing to the negative plane are almost the same in this energy region

Figure 13 compares MC results for B profiles ion implanted at 20, 40, and 80 keV with Pearson function using its moment parameters. They agree well and hence using raw data of moment parameters gives accurate Pearson function as well as the low-energy region, as shown in Fig 11. The moment parameter values are almost invariant, independent of the MC simulation mode of tracing or non-tracing in this energy region.

Figure 14(a) shows (γ^2, β) extracted from Monte Carlo data of ion implanted profiles in Si and Ge substrates with the energy region up to 320 keV. It is noteworthy that they are almost on the line of

$$\beta = 2.661 + 1.852\gamma^2 \tag{44}$$

and also that (γ^2, β) is always outside Pearson IV region.

Figure 14(b) shows the (γ^2, β) extending for B profiles the energy region up to 5000 keV. It is noteworthy that the simple extension of Eq. 44 to the higher γ^2 region is invalid, and further (γ^2, β) breaks the limitation of Pearson function. Therefore, the simple use of moment parameters is obviously invalid in high-energy region.

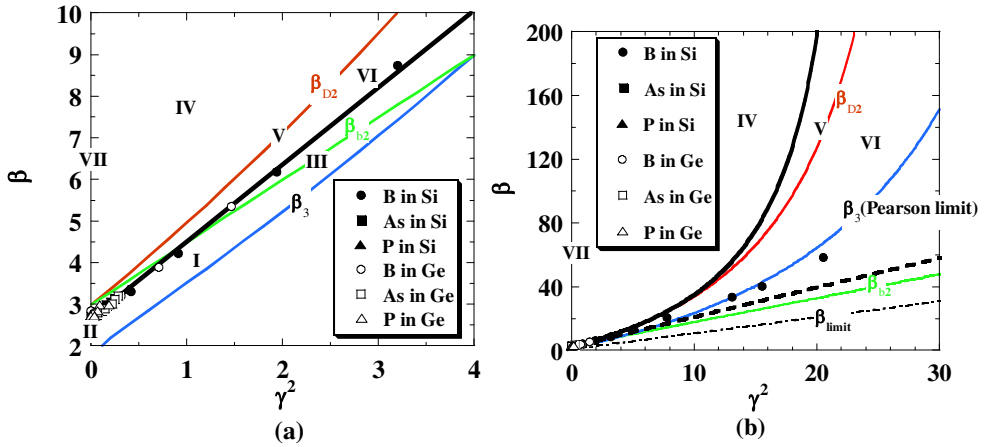

Fig. 14. $\gamma^2 - \beta$ Relationship for various ion and Si and Ge substrates. (a) Energy region less than 360 keV. (b) Energy up to 5000 keV for B.

Based on the above data, we compare the MC data with Pearson using raw moment data, and Pearson IV with β forcing to β_{D2} of Eq. 32, as shown in Fig. 15.

The profile at an energy of 0.5 keV is symmetrical, that is, $|\gamma|$ of the profile is small. The Pearson function using raw moment parameters effectively reproduces the MC data, while the Pearson IV profile deviates from the MC data in the low tail concentration region. The MC profile at 80 keV becomes asymmetrical, and the Pearson profile deviates from the MC data, and MC data is in between the Pearson and Pearson IV profiles. When we further increase the energy to 160 keV, the Pearson profile becomes inaccurate, and Pearson IV becomes better. Further, the Pearson profile clearly becomes inaccurate even in the peak region at 1000 keV, while Pearson IV readily reproduces the MC data. Consequently, the MC results can be well expressed by Pearson function using raw moment parameters when the profile is symmetrical and Pearson IV is inaccurate and vice versa when the profile is asymmetrical.

We think that the above information can be appreciated with the following.

The moments of the profile can be defined for any order, as shown in Eq. 13, while Pearson function uses only the first four moments. When a profile is rather symmetrical, it can be accurately expressed using the first four moment parameters, and the direct use of the moment values can generate the profile accurately, and different moment parameters such as those for Pearson IV induce inaccurate one. This is the case for low energy. When the profile is rather asymmetrical, the four moments are not enough to express the profile, that is, Pearson function is not available if we use original moment values. If we limit ourselves to use Pearson function, we should use moments different from the raw ones to improve the accuracy approximately. One way to modify the parameter is to increase β although we do not understand its mathematical reason. If we use Pearson IV in this case, we use larger β than the raw ones, which ensure better agreement. This is the case for high energy. Therefore, Pearson IV expresses the profile more accurately than the Pearson using the raw moment values in this case.

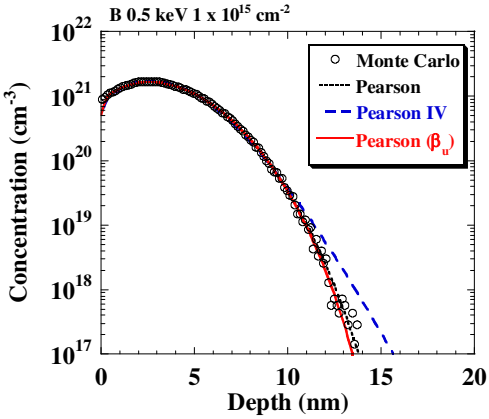
B 0.5 keV 1 x 10^15 cm^-2
Monte Carlo
Pearson
Pearson IV
Pearson (β_u)
Concentration (cm^-3)
Depth (nm)

(a)

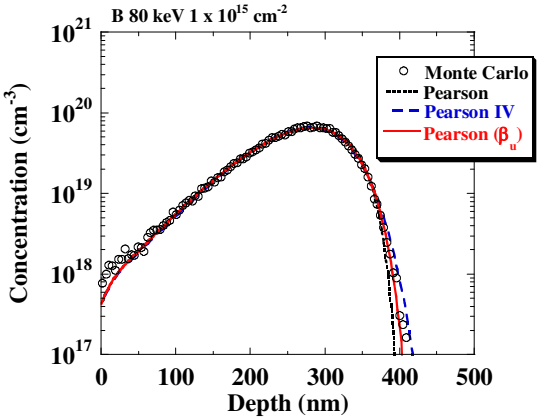
B 80 keV 1 x 10^15 cm^-2
Monte Carlo
Pearson
Pearson IV
Pearson (β_u)
Concentration (cm^-3)
Depth (nm)

(b)

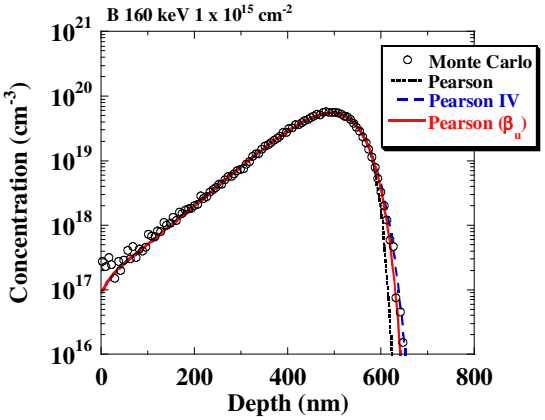
B 160 keV 1 x 10^15 cm^-2
Monte Carlo
Pearson
Pearson IV
Pearson (β_u)
Concentration (cm^-3)
Depth (nm)

(c)

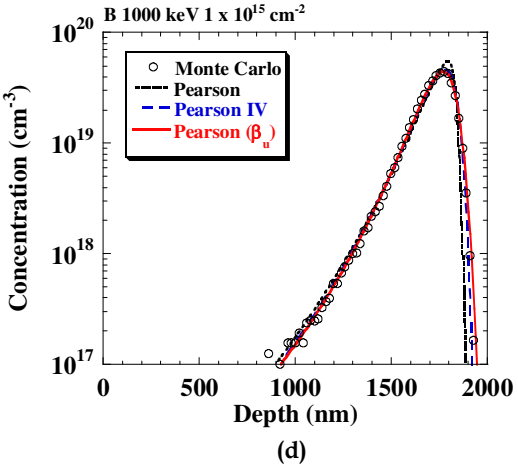

Fig. 15. MC simulation of B ion implantation profiles in Si substrates. Pearson function using raw moment parameters, and moment parameters of MC tracing to the negative plane are also shown The Pearson using the proposed B is also shown. (a) 0.5 keV, (b) 80 keV, (c) 160 keV, and (d) 1000 keV.

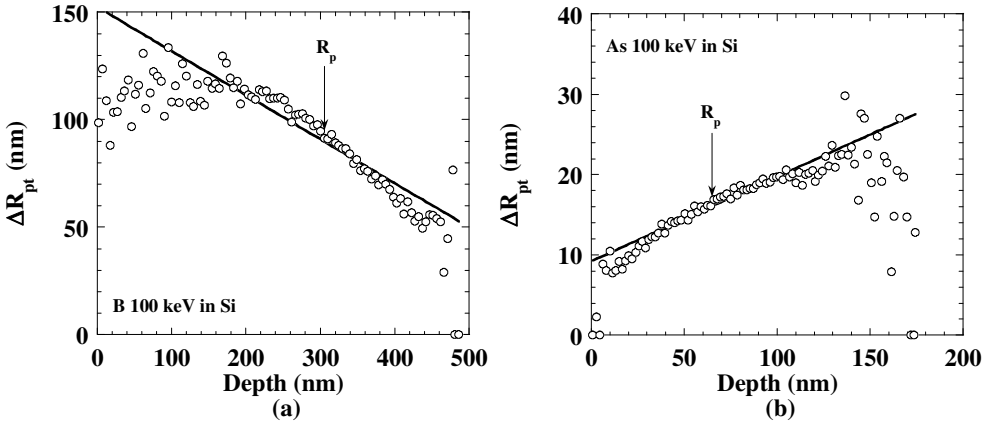

Fig. 16. Depth dependent lateral straggling.

Based on the above information, we propose to use β of

$$\beta_u = \frac{25\left(2.661 + 1.852\gamma^2\right)}{25 - \gamma^2} \tag{45}$$

We denote this β as β_u. β_u is shown in Fig. 14 as a solid line, and it is almost the same as Eq. 44 in low-energy ranges, as shown in Fig. 14(a), and it enters the Pearson IV domain for large γ^2, as shown in Fig. 14 (b). Figure 15 also shows the profiles using β_u, where any MC profile can be accurately expressed.

We can also evaluate lateral straggling ΔR_{pt} from the MC results by integrating over the lateral direction. It is also pointed out that the lateral straggling depends on depth [Suzuki (2001)]. Figure 16 shows evaluated lateral straggling of B and As ion implantation. ΔR_{pt} decreases with depth for B, and increases for As. It is clear that the lateral straggling depends on the depth linearly near the depth of R_p. Therefore, we evaluate the lateral straggling as

$$\Delta R_{pt} = \Delta R_{pt0} + m\left(x - R_p\right), \tag{46}$$

where ΔR_{pt0} is the ΔR_{pt} at R_p. Using the form of Eq. 46, we can extract m from the MC results. Figure 16 also shows the extracted ΔR_{pt} as solid lines.

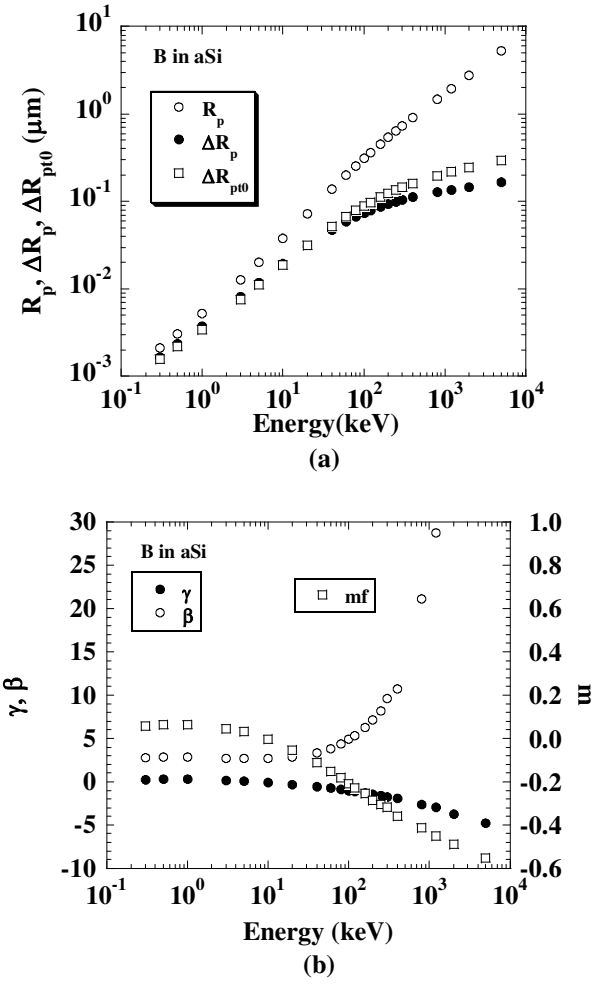

Fig. 17. Moment parameters of B ion implantation profiles.

Using the above procedure of MC tracing to the negative plane and β_u, we can establish a database of B, P, As, In, and Sb In ion implantation, as shown in Figs. 17, 18, 19, 20, 21, respectively. Using the database, we can generate ion implantation profiles instantaneously for any ion implantation conditions.

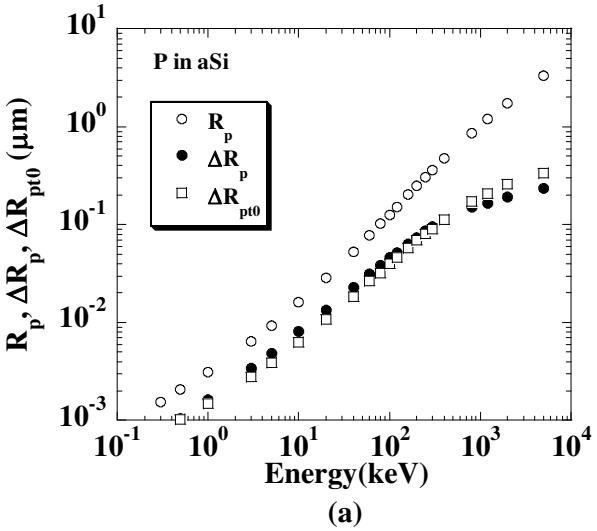

Fig. 18. Moment parameters of P ion implantation profiles.

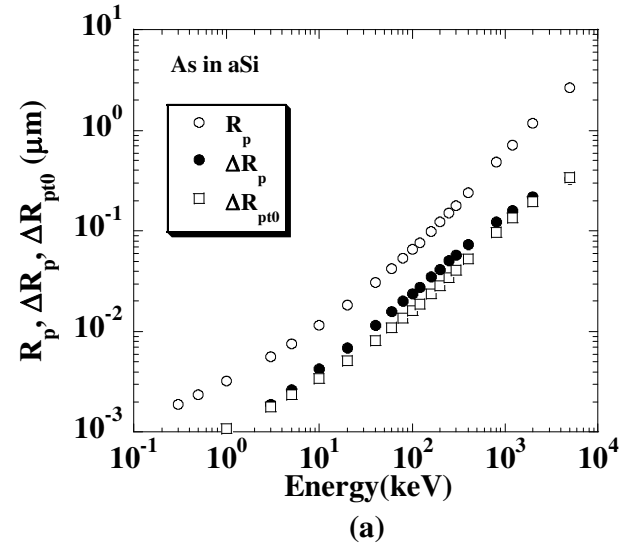

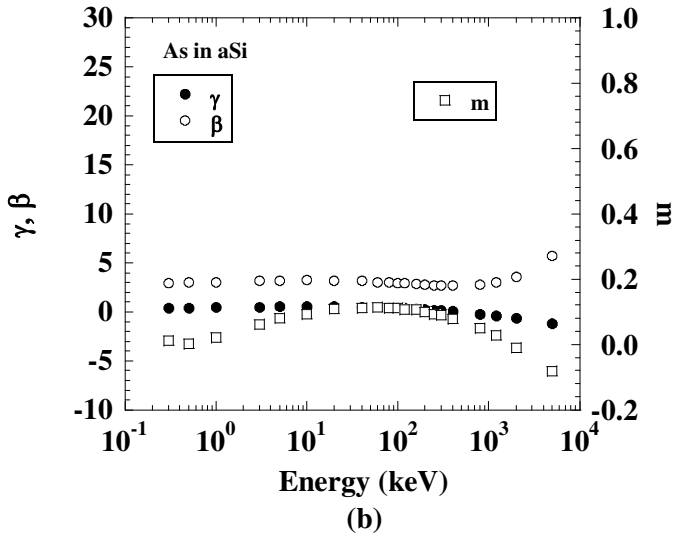

Fig. 19. Moment parameters of As ion implantation profiles.

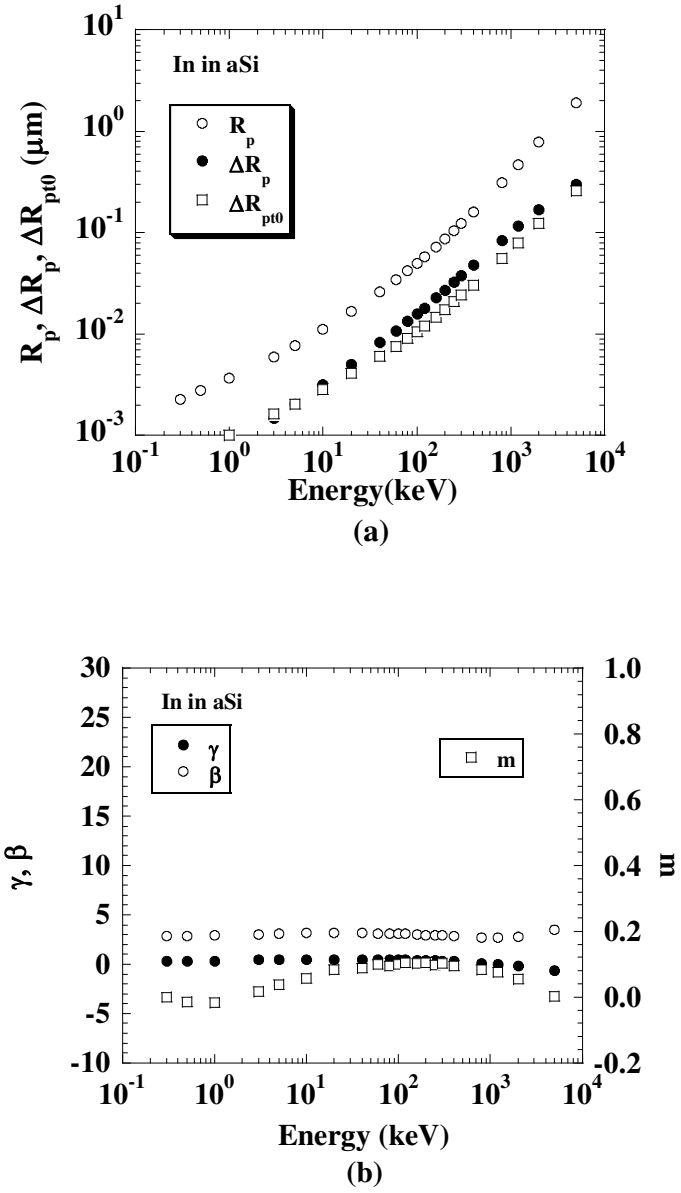

Fig. 20. Moment parameters of In ion implantation profiles.

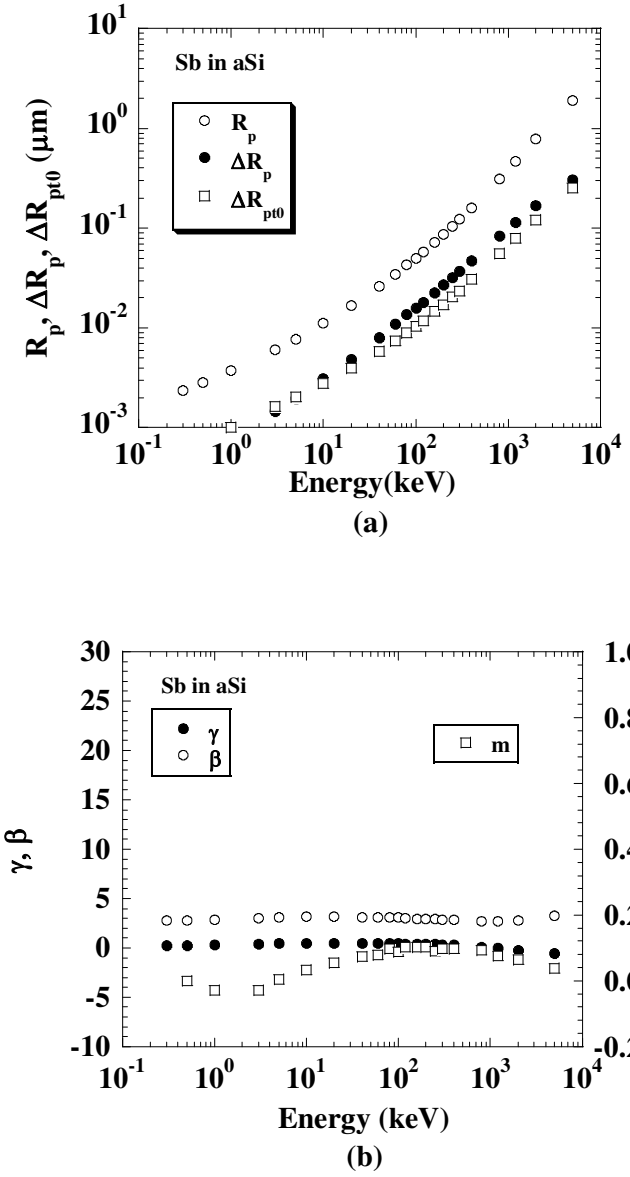

Fig. 21. Moment parameters of Sb ion implantation profiles.

6. Comparison of MC with TEM data

Figure 22 shows the cross-sectional TEM image of the amorphous layer formed by Ge ion implantation at an energy of 10 keV and various doses. We do not observe continuous amorphous layer at a dose of 10^{13} cm^{-2}, continuous amorphous layer with a thickness d_a of 9.4 nm at a dose of 10^{14} cm^{-2} with non-clear amorphous/crystal (a/c) interface, larger d_a of 20.2 nm with clear a/c interface at a dose of 10^{15} cm^{-2}, and further larger d_a of 24.5 nm with clear a/c interface at a dose of 5×10^{15} cm^{-2}.

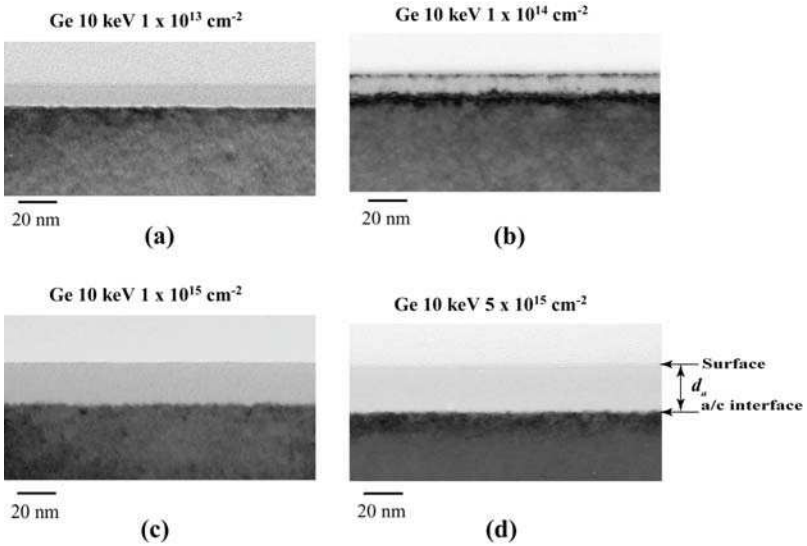

Fig. 22. Cross-sectional TEM image of the amorphous layer formed by Ge ion implantation.

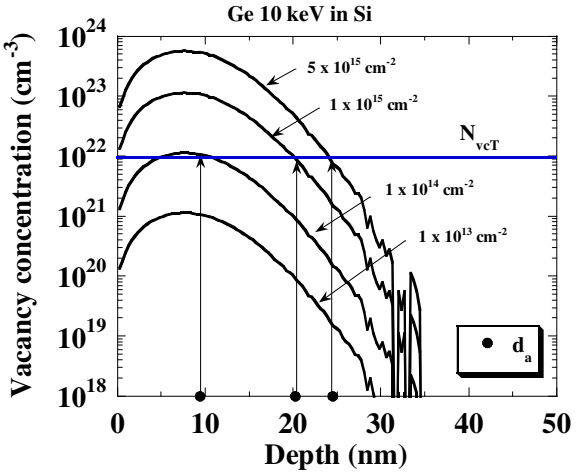

Fig. 23. Vacancy concentration induced by Ge ion implantation.

MC can evaluate accurately the transferred energy and vacancy concentration, as shown in Section 3. It should be noted that MC cannot predict absolute vacancy concentration since it does not consider temperature and hence the recombination of generated vacancy and recoiled substrate atoms. However, MC results neglecting the recombination may be able to be related to the amorphous layer thickness empirically.

Figure 23 shows the vacancy concentration evaluated by MC with the tracing mode. The amorphous layer thicknesses evaluated from Fig. 22 are also shown. It is noteworthy that the vacancy concentration at depth of d_a is almost the same, independent of dose. Therefore, we may relate d_a to the critical vacancy concentration denoted by N_{vcT}. This also well explains that the continuous amorphous layer is not formed with a dose of 10^{13} cm^{-2} since the peak vacancy concentration is lower than N_{vcT}.

It is also interesting that d_a is near the peak region at a dose of 10^{14} cm^{-2} where is the vacancy concentration is still high ever deeper than d_a. On the other hand, the gradient of vacancy concentration is high for the doses of 1×10^{15} cm^{-2} and 5×10^{15} cm^{-2}. This means that the vacancy concentration decreases drastically in the deeper region than d_a. Therefore, the clearness of the a/c interface can be related to the gradient of the vacancy concentration at d_a.

Figure 24 shows the comparison of the amorphous layer thickness with the vacancy concentration for various ions and energies. It is noteworthy that the vacancy concentration at a depth of d_a is almost the same, independent of energy, as shown in Fig. 23, but it depends on ions. In the MC simulation, the two types of MC calculation mode of tracing and non-tracing are shown. When we trace the recoiled substrate atom, we denote it as T.

There is no significant difference between tracing and non-tracing mode when the ion is light as B, but the difference becomes significant when the ion is heavy as As. The trajectories of B and As implanted in Si substrate are shown in Fig. 25 as black dotted lines, and recoiled Si trajectories are shown as yellow dotted lines. The recoiled Si does not go far from the ion trajectory path of B, and the distribution of vacancy for both modes are almost the same. While the recoiled Si goes far from the As trajectory path and generates much more recoiled Si, the profile of recoiled Si distribution is significantly different from the ion trajectory site. This is the reason why the vacancy distributionshows difference in the two modes.

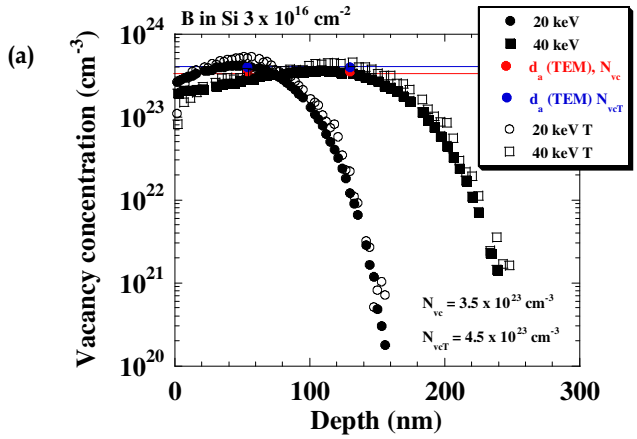

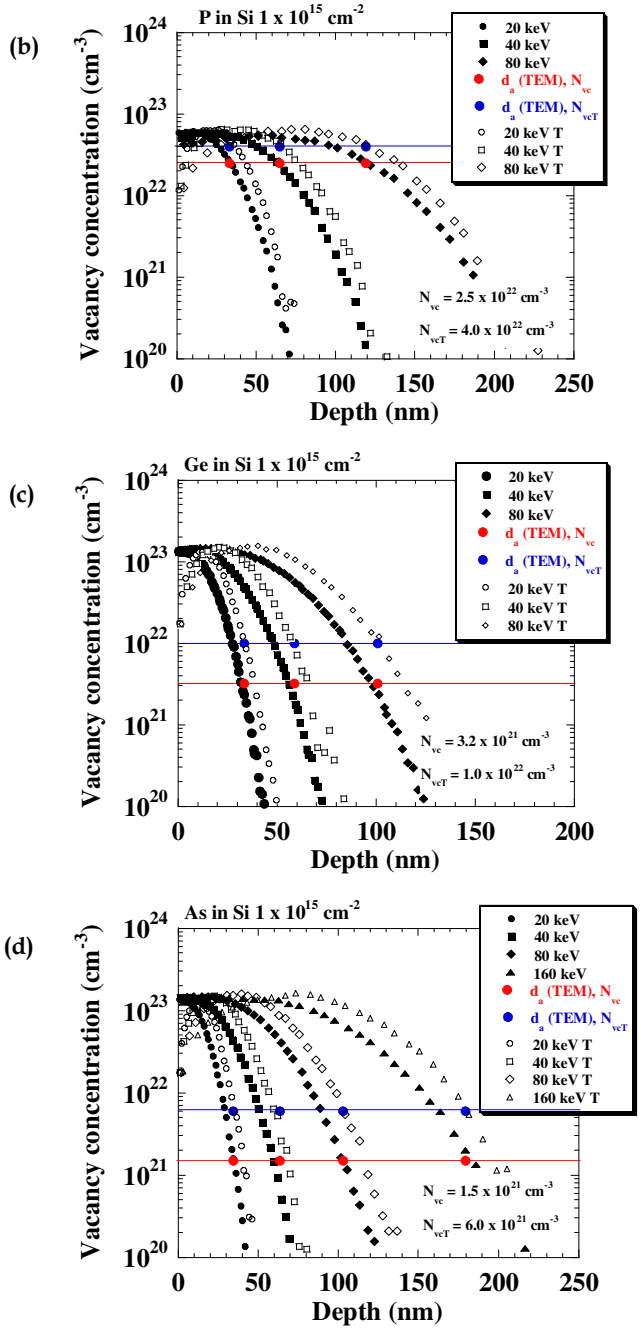

Fig. 24. Vacancy concentration with two modes: Tracing and non-tracing modes. (a) B in Si, (b) P in Si, (c) Ge in Si, (d) As in Si.

Therefore, the critical concentration of vacancy at the a/c interface is different although both are rather independent of energy. It is noteworthy that the vacancy concentration at the a/c interface is almost constant for each trace mode although the value is different in some cases. Therefore, we can predict d_a by evaluating the vacancy concentration in the MC simulation with both modes although the tracing mode is more physical.

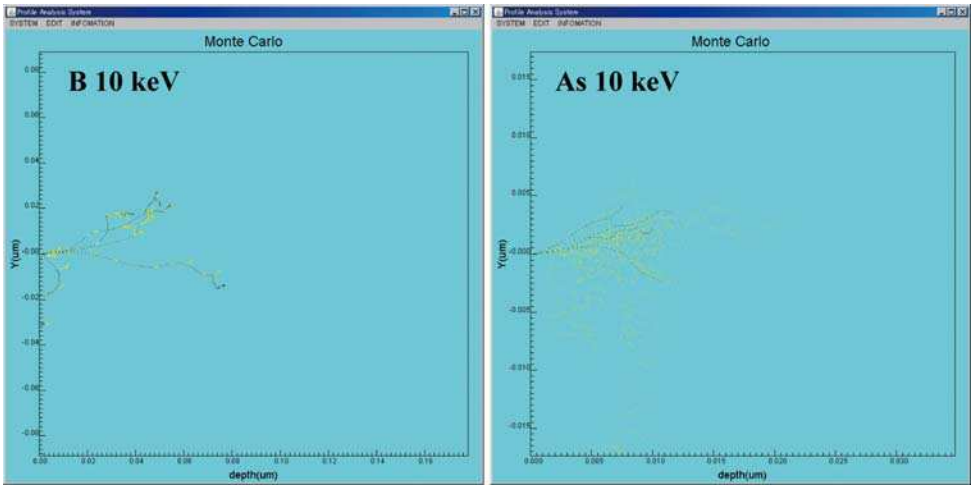

Fig. 25. MC simulation with tracing mode. B and As trajectories are shown. Black dotted lines correspond to the ion trajectories, and yellow ones to recoiled Si.

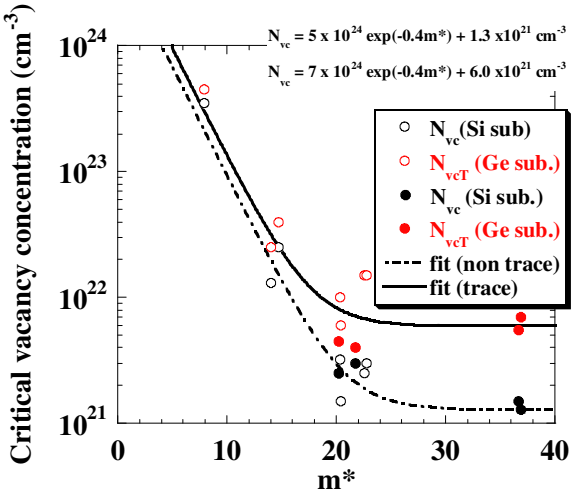

Fig. 26. Dependence of critical vacancy concentration on reduced mass.

We hope to predict d_a for an unknown incident ion and substrate system. Fig. 26 shows the dependence of critical vacancy concentration on reduced mass. Any point is almost on lines of

$$N_{vc} = 5\times10^{24}\exp\left(-0.4m^*\right) + 1.3\times10^{21}\ cm^{-3} \tag{47}$$

$$N_{vcT} = 7\times10^{24}\exp\left(-0.4m^*\right) + 6.0\times10^{21}\ cm^{-3}, \tag{48}$$

where m^* is the reduced mass defined by

$$\frac{1}{m^*} = \frac{1}{m_1} + \frac{1}{m_{sub}}, \tag{49}$$

although the physical reason is not clear, we can use Eqs. 47 and 48 to predict d_a as the initial guess of amorphous layer thickness by MC.

Prussin also analyzed the amorphous layer thickness based on Brices's energy deposition model. They also used critical deposition energy like N_{vc} or N_{vcT} in Cerva and our analysis. Cerva used the same N_{vcT} for P and As in Si substrate. However, we used a different one, and it is also different in ref. [Prussin (1984)]. The dependence becomes more clear when we used a light ion such as B whose N_{vc} or N_{vcT} is quite high in our analysis and also in Prussin (1984), while Cerva uses the constant N_{vcT}, independent of ions. We think that our result is plausible since B does not recoil Si atom so far from the original lattice site, and recombination aptly occurs through self annealing.

Prussin also expressed the amorphous layer thickness d_a with an empirical form of

$$d_a = R_p + n\Delta R_p, \tag{50}$$

where n is the fitting parameter and changes with ions and dose. We applied physical appreciation to Eq. 50 and proposed the modified one as

$$d_a = \begin{cases} R_p + \sqrt{2}\Delta R_p erfc^{-1}\left(\dfrac{2\Phi_{\%_c}}{\Phi}\right) & \Phi \geq 2\Phi_{\%_c} \\ 0 & \Phi < 2\Phi_{\%_c} \end{cases}, \tag{51}$$

where Φ is the dose and $\Phi_{\%_c}$ is the through dose defined by

$$\Phi_{\%_c} = \int_{d_a}^{\infty} N(x)dx, \tag{52}$$

where $N(x)$ is the ion concentration. $\Phi_{\%_c}$ is regarded as constant if the ion and substrate are defined independent of energy and dose. If we assume Gaussian profile, we can perform the integration and obtain the analytical form as

$$\begin{aligned} \Phi_{\%_c} &= \int_{d_a}^{\infty} \frac{\Phi}{\sqrt{2\pi}\Delta R_p}\exp\left[-\left(\frac{x-R_p}{\sqrt{2}\Delta R_p}\right)^2\right]dx \\ &= \frac{\Phi}{2}erfc\left(\frac{d_a - R_p}{\sqrt{2}\Delta R_p}\right) \end{aligned} \tag{53}$$

Let us combine this formula to MC. We then analyze Ge ion implantation. We can predict d_a = 59 nm, R_p = 31.5 nm, and ΔR_p = 12.0 nm for Ge ion implantation at 40 keV with a dose of $1\times10^{15} cm^{-2}$ from the MC simulation. Substituting these parameters to Eq. 53, we obtain $\Phi_{a/c} = 1.1\times10^{13} cm^{-2}$. We then use this for any ion implantation condition of dose and energy. Figure 27 compares the experimental and theoretical amorphous layer thicknesses. We obtained a good agreement over the wide ion implantation condition. The agreement is rather bad for a dose of 10^{14} cm^{-2}. However, the a/c interface is not clear for this dose.

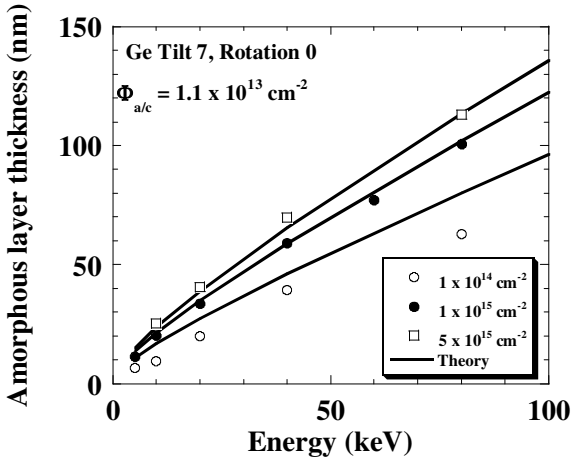

Fig. 27. Comparison of experimental d_a with the theoretical model using fixed $\Phi_{a/c} = 1.1\times10^{13} cm^{-2}$.

In our analysis, we neglect the channeling phenomenon, which is a prominent feature for profiles in crystalline substrates. Although the channeling effect may be significant for the profiles in cSi, our successful analysis means that channeling is obviously negligible for the amorphization. This can be explained by the small fraction of channeling ions and by the fact that damage is primarily produced by non-channeling ions.

7. Conclusion

We showed that Monte Carlo simulation is vital to predict ion implantation profiles as well as amorphous layer thickness resulting from ion implantation. The MC results for ion implantation profiles deviate from the experimental data in some cases as it is. However, if we tune the parameter of electron stopping power for one energy, we can accurately predict the profiles for any energy. The ion implantation profiles for the high-energy region cannot be well reproduced by Lindhard electron stopping power model, but it can be reproduced by using the combined model of Lindhard and modified Bethe models. We also showed how to extract the parameters of MC data to generate the Pearson function. Simple use of moment parameters induces error in some cases, and we propose the MC tracing to the negative plane, and universal β instead of its raw value. We also showed that the forcing Pearson IV function is valid in the high-energy region where the profile is rather

asymmetrical, but it induces error in the low-energy region where the profile is rather symmetrical. We can simply predict the amorphous layer thickness by evaluating the vacancy concentration. The critical vacancy concentration depends on the calculation method: tracing or non-tracing mode, but the value is independent of energy for both modes. We proposed the empirical critical vacancy concentration, and d_a for any combination of incident ion and substrate atoms can be predicted using this. We can also evaluate a parameter of through dose $\Phi_{\%_c}$ by MC. Using the $\Phi_{\%_c}$ combined with the database for moment parameters of the profile based on the MC, we can predict d_a instantaneously without using MC afterward.

8. References

Ashworth D. G., Oven R., and Mundin B. (1990), Appl. Phys. D., vol. 23, pp. 870-876.

Bethe H. A. (1930), Ann. Phys. (Leipzig), vol. 5, pp. 325-400.

Biersack J. P., and Haggmark L. G.(1980), Nuclear Inst. And Meth., vol. 174, pp. 257-269.

Brice K. B. (1975), *Ion implantation range and energy deposition distribution*, IFI/Plenum Publishing Corporation, ISBN: 0-306-67401-7, London.

Cerva H., and Hobler G. (1992), J. Electrochem. Soc., vol. 139, No. 12, pp. 3631-3638.

Chui C. O., Ramanathan S., Triplett B. B., McIntyre P. C., and Saraswat K. C. (2002), IEEE Electron Device Lett., EDL-23, No. 8, pp. 473-475.

Dalton P. and Turner J. E., (1968), Health Physsics Pergamon Press, vol. 15, pp. 257-262.

FabMeister-IM: http://www.mizuho-ir.co.jp/english/solution/ion/index.html

Hobler G. and Selberherr S. (1988), IEEE Trans on Computor-Aided Desing, vol. 7, No.2, pp. 174-180, 1988.

Hofker W. K. (1975), Philips Res. Rep. Suppl., vol. 8, pp. 1-121.

Holmstrom E., Kuronen A., and Nordlund K. (2008), Physical Review B, vol 78, 045202.

Hu J. C., Chaterjee A., Mehrotra M., XuJ., Shiau W. –T., and Rodder M. (2000), Proceedings of Symposium on VLSI Tech., pp. 188-189. Honolulu, June 13-15, 2000.

Jin J.-Y., Liu J., Jeong U., and Mehta S. (2002), J. Vac. Sci. Technol. B, Vol. 20, pp. 422-426.

Kataoka Y. and Itani T. (2007), Surf. Interface Anal., vol. 39, pp. 826-831.

Kim Y. S., Shimamune Y., Fukuda M., Katakami A., Hatada A., Kawamura K., Ohta H., Sakuma T., Hayami Y., Morioka H., Ogura J., Minami T., Tamura N., Mori T., Kojima M., Sukegawa K., Hashimoto K., Miyajima M., Satoh S., and Sugii T. (2006), Proceedings of Electron Devices Meeting, pp. 622-625. ISBN: 1-4244-0438-x, SanFrancisco, December 11-13, 2006.

Lindhard J., and Scharff M. (1961), Phys. Rev., Vol. 124, No. 1, pp. 128-130.

Mirabera S., Impellizzeri G., Bruno E., Romano L., Grimaldi M. G., and Priolo F., Napolitani E., and Carnera A. (2005), Appl. Phys. Lett., vol. 86, 121905.

Pawlak B. J., Vandervorst W., Smith A. J., Cowern N. E., Colombeau B., and Pages X. (2005), Appl. Phys. Lett., Vol. 86, 101913.

Prussin S., Margolese D. I., and Tauber R. N. (1984), J. Appl. Phys. Vol. 57, No. 2, pp. 180-185. Sentaurus Process http://www.synopsys.com/Tools/TCAD/ ProcessSimulation/Pages/SentaurusProcess.aspx

Selberherr S. (1984), *Analytsi and simulation of semiconductor device*, Springer-Verlag, ISBN: 3-211-81800-6, Wien.

Shang H., Okorn-Schmidt H., Ott J., Kozlowski P., Steen S., Jones E. C., Wong H.-S. P., and Hanesch W.(2003), IEEE Electron Device Lett., EDL-24, No. 4, pp. 242-244.

Schoerner R., Friedrichs P., Peter D., and Stephani D. (1999), IEEE Electron Device Lett., EDL-20, No. 5, pp. 241-244.
Solmi S., Landi E., and Baruffaldi F. (1990), J. Appl. Phys., pp. 3250-3258.
SRIM-2003: http://www.srim.org/
Suzuki K., Sudo R., Tada Y., Tomotani M., Feudel T., and Fichtner W. (1998),
Solid-State Electronic, vol. 42, pp. 1671-1678.
Suzuki K., Sudo R, and Nagase M. (2001), IEEE Trans. Electron Devices, ED-48, pp. 2803-2807.
Suzuki K. and Tashiro H. (2003), IEEE Trans. Electron Devices, ED-50, pp. 1753-1757.
Suzuki K., Tashiro H., Narita K., and Kataoka Y. (2004), IEEE Trans. Electron Devices, ED-51, pp. 663-668.
Suzuki K., Kawamura K., Kikuchi Y., and Kataoka Y. (2006), IEEE Trans. Electron Devices, vol. ED-53, NO. 5, pp. 1186-1192.
Suzuki K., Tada Y., Kataoka Y., and Nagayama T. (2009), J. Semiconductor Technology and Science, vol.9, No. 1, pp. 67-74.
Suzuki K. (2010a), Fujitsu Scientific & Technical Journal, vo. 46, No. 3, pp. 307-317.
Suzuki K., Tada Y., Kataoka Y., and Kojima S. (2010b),Proceedings of 18th Ion Implantation Tech.,P2-24, Kyoto, June 6-11, 2010.
Tada Y., Suzuki K., and Kataoka Y. (2008), Applied Surface Science, vol. 255, pp. 1320-1322.
Tian S. (2003), J. Appl. Phys., vol. 93, No. 10, pp. 5893-5904.
Weber O., T. Irisawa, Numata T., Harada M., Taoka N., Yamashita Y., Yamamoto T., Sugiyama N., Takenaka M., and Takagi S. (2007), Proceedings of Electron Devices Meeting, pp. 719 – 722. ISBN: 1-4244-1507-1, Washington DC, December 10-12, 2007.
Ziegler J. F., Biersack J. P., and Litmark U. (2008), *SRIM The Stopping and Ranges of Ions in Matter*, SRIM Co., ISBN: 0-9654207-1-x, USA.

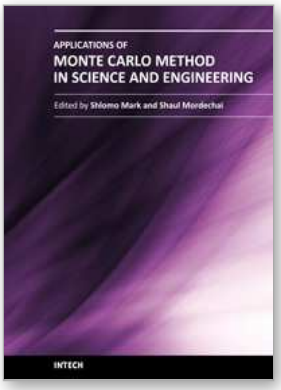

Applications of Monte Carlo Method in Science and Engineering

Edited by Prof. Shaul Mordechai

ISBN 978-953-307-691-1
Hard cover, 950 pages
Publisher InTech
Published online 28, February, 2011
Published in print edition February, 2011

In this book, Applications of Monte Carlo Method in Science and Engineering, we further expose the broad range of applications of Monte Carlo simulation in the fields of Quantum Physics, Statistical Physics, Reliability, Medical Physics, Polycrystalline Materials, Ising Model, Chemistry, Agriculture, Food Processing, X-ray Imaging, Electron Dynamics in Doped Semiconductors, Metallurgy, Remote Sensing and much more diverse topics. The book chapters included in this volume clearly reflect the current scientific importance of Monte Carlo techniques in various fields of research.

How to reference

In order to correctly reference this scholarly work, feel free to copy and paste the following:

Kunihiro Suzuki (2011). Monte Carlo Simulation for Ion Implantation Profiles, Amorphous Layer Thickness Formed by the Ion Implantation, and Database Based on Pearson Function, Applications of Monte Carlo Method in Science and Engineering, Prof. Shaul Mordechai (Ed.), ISBN: 978-953-307-691-1, InTech, Available from: http://www.intechopen.com/books/applications-of-monte-carlo-method-in-science-and-engineering/monte-carlo-simulation-for-ion-implantation-profiles-amorphous-layer-thickness-formed-by-the-ion-imp

INTECH
open science | open minds

InTech Europe
University Campus STeP Ri
Slavka Krautzeka 83/A
51000 Rijeka, Croatia
Phone: +385 (51) 770 447
Fax: +385 (51) 686 166
www.intechopen.com

InTech China
Unit 405, Office Block, Hotel Equatorial Shanghai
No.65, Yan An Road (West), Shanghai, 200040, China
中国上海市延安西路65号上海国际贵都大饭店办公楼405单元
Phone: +86-21-62489820
Fax: +86-21-62489821